# Ceramics



# In situ investigation of atmospheric plasma-sprayed Mn–Co–Fe–O by synchrotron X-ray nano-tomography

Nikolas Grünwald<sup>1,\*</sup> , Pierre Lhuissier<sup>2</sup>, Luc Salvo<sup>2</sup>, Julie Villanova<sup>3</sup>, Norbert H. Menzler<sup>1</sup>, Olivier Guillon<sup>1,4</sup>, Christophe L. Martin<sup>2</sup>, and Robert Vaßen<sup>1</sup>

Received: 23 April 2020 Accepted: 2 June 2020

© The Author(s) 2020

#### **ABSTRACT**

Applying atmospherically plasma-sprayed (APS) Mn<sub>1.0</sub>Co<sub>1.9</sub>Fe<sub>0.1</sub>O<sub>4</sub> (MCF) protective coatings on interconnector steels minimized the chromium-related degradation within solid oxide fuel cell stack-tests successfully. Post-test characterization of the coatings disclosed a severe microstructural and phase evolution. A self-healing of micro-cracks, the formation and agglomeration of small pores, the occurrence of a dense spinel layer at the surface and a strong elemental de-mixing were reported in ex situ experiments. In the present publication, we prove for the first time these mechanisms by tracking the microstructure in situ at a single APS coating using synchrotron X-ray nanotomography at the European Synchrotron Radiation Facility. Therefore, a 100-µm-long cylindrical sample with a diameter of  $123 \,\mu m$  was cut from an APS-MCF free-standing layer and measured within a high-temperature furnace. All microstructural changes mentioned above could be verified. Porosity measurements reveal a decrease in the porosity from 9 to 3% during the annealing, which is in good accordance with the literature. Additionally, a partial detachment of an approximately 5-µm-thick layer at the sample surface is observed. The layer is dense and does not exhibit any cracks which are penetrating the layer. This kind of shell is assumed to be gastight and thus protecting the bulk from further oxidation.

Address correspondence to E-mail: nikolas.gruenwald@gmx.net

Published online: 19 June 2020

https://doi.org/10.1007/s10853-020-04916-9



<sup>&</sup>lt;sup>1</sup>Forschungszentrum Jülich GmbH, Institute of Energy and Climate Research (IEK), IEK-1: Materials Synthesis and Processing, Wilhelm-Johnen-Straße, 52425 Jülich, Germany

<sup>&</sup>lt;sup>2</sup>CNRS, SIMAP, University of Grenoble Alpes, 38000 Grenoble, France

<sup>&</sup>lt;sup>3</sup>ID16B - ESRF - The European Synchrotron, CS40220, 38043 Grenoble, Cedex 9, France

<sup>&</sup>lt;sup>4</sup> Jülich Aachen Research Alliance, JARA-Energy, Aachen, Germany

#### Introduction

Chromium-containing steels are widely used as interconnector material in solid oxide fuel cells (SOFCs) [1, 2]. They provide sufficient electronic conductivity and chemical stability in reducing and oxidizing atmospheres at temperatures between 600 and 900 °C [3, 4]. Additionally, these materials are easy to manufacture and exhibit a high toughness compared to previously used ceramics. The major disadvantage of chromium-containing steels arises from the evaporation of chromium-containing oxides at the high operation temperatures of SOFCs [5, 6]. The reaction of these gaseous chromium species with commonly used cathode materials like (La,Sr)MnO<sub>3</sub> (LSM) or  $La_{1-x}Sr_xFe_{1-y}Co_yO_3$  (LSCF) leads to a strong voltage degradation of SOFC stacks [7–9]. The amount of evaporating chromium is highly dependent on the oxide scale that is formed on the surface of the steels during operation and on the existing atmosphere [10]. In case of oxidizing pure chromium or chromium base alloys, a Cr<sub>2</sub>O<sub>3</sub> layer is formed exhibiting a high chromium evaporation rate. By adjusting the steel composition, the oxide scale can be optimized to reduce the evaporation rate of chromium species. Adding manganese as dopant leads to the formation of a double oxide layer [3, 11]. A chromium manganese spinel is covering the Cr<sub>2</sub>O<sub>3</sub> layer which reduces the evaporation of gaseous chromium species [5, 12] and minimizes the oxidation rate in addition.

Applying chromium protection layers on already optimized interconnector steels can further decrease the amount of evaporating chromium species [13, 14]. They can be categorized into two groups according to their protection mechanism. Firstly, porous layers can be adapted to chemically bind volatile chromium species [15–17]. Although these protective layers cannot completely retain gaseous chromium species and have only a limited absorption capacity, which leads to a limited stack lifetime, they are often applied in industry due to low manufacturing costs. Coatings of the second group protect the cathode by acting as a physical barrier. As these coatings are dense and gastight, gaseous chromium species cannot reach the cathode via the gas phase [16]. Additionally, the oxidation of the interconnector is reduced.

The efficient reduction in degradation using dense protective layers induced a broad research on a large number of different materials and manufacturing techniques [18, 19]. Due to the high operation temperature of SOFCs, a thermal expansion coefficient that is matching to the adjacent functional layers and the interconnect is as essential for protective coatings as their chemical stability in oxidizing atmosphere and a high electronic conductivity. Fulfilling these demands, Mn<sub>1.0</sub>Co<sub>1.9</sub>Fe<sub>0.1</sub>O<sub>4</sub> (MCF) was tested as material in combination with various application techniques, as there are atmospheric plasma spraying (APS) [20–26], wet powder spraying [27, 28], aerosol deposition [18], physical vapor deposition [29] and electrophoretic deposition [14]. Compared to the others, APS combines the advantageous of achieving high density without sintering steps and relatively low manufacturing costs. SOFC stacks operated with atmospheric plasma-sprayed Mn<sub>1.0</sub>Co<sub>1.9</sub>Fe<sub>0.1</sub>O<sub>4</sub> (APS-MCF) protection layers revealed a low degradation rate, which could be related to a negligible chromium poisoning of the cathode material in post-test analyses [30].

Further investigations of APS-MCF coatings before and after annealing in air simulating the cathodic **SOFC** operation conditions revealed microstructural and phase changes. Focusing on the microstructure, the healing of micro-cracks after short annealing in air above 350 °C was observed [22, 31]. The formation of a dense layer of material at the surface was documented, when the annealing is continued and the annealing temperature is increased [31]. An increase in porosity can be detected after long-term annealing at 850 °C. Phase analyses by X-ray diffraction (XRD) showed that a phase transformation from the spinel-type raw powder to a rock salt phase in the deposited state of the MCF coating occurs [22, 23, 32]. Annealing the APS-MCF samples in air lead to a phase transformation back to the spinel phase, which can be identified as the lowtemperature stable configuration by the phase diagram given in [33]. The phase transformation induces diffusion processes, which are described in detail in [31]. All microstructural investigations that are described in the cited articles have been performed ex situ on different samples. Thus, all observations are based on the assumption that the microstructure of the investigated samples was similar in the initial state after APS.



In the present work, these microstructural changes of APS-MCF are verified by 3D in situ imaging. For this purpose, synchrotron X-ray nano-tomography (SXNT) measurements were performed at the beamline ID16B at the European Synchrotron Radiation Facility (ESRF) in Grenoble (France). The device allows ultra-fast scans with acquisition times less than a few seconds for small samples [34–36]. In case of thicker samples (more than 100 μm) which are necessary for the investigation of APS-MCF, an acquisition time of less than 10 min and a voxel resolution of 75 nm can be achieved. The reported selfhealing of micro-cracks can be monitored in situ and traced over the annealing procedure within the recorded tomograms. Due to the high spatial resolution of the device, even nano-structured changes can be detected during high-temperature annealing.

## **Experimental**

The optimal sample geometry for SXNT measurements of MCF was determined to a cylinder with a diameter of 125 μm and a length of more than 50 μm by preliminary tests and calculations. To obtain such defined sample geometries, a free-standing APS-MCF layer was used as bulk material, which was processed afterward. A spinel-type manganese-cobaltiron oxide powder (H.C. Starck, Laufenburg, Germany) with the following chemical composition was used as raw material for the APS process: 23.5 wt% Mn, 47.6 wt% Co, 2.4 wt% Fe and 26.5 wt% O. More information about the spray process is given in [22, 23, 31]. Free-standing layers were manufactured by spraying MCF with a thickness of 150 μm on a salt-coated steel substrate and subsequent dissolution of the salt in water. A micro-drill (Medenbach, Bochum, Germany) was used to cut the layer to a truncated cone-shaped geometry with a length of 150 μm, an upper diameter of 191 μm and a lower diameter of 275 µm. After this pre-preparation, the sample was placed on the tip of a 50-mm-long alumina stick with a diameter of 1.5 mm (Friatek, Mannheim, Germany) using the ceramic glue Ceramabond 685 N (Kager GmbH, Dietzenbach, Germany) (Supplementary 1). Subsequent fine-tuning of the sample geometry was performed with focused ion beam (FIB) technology (Helios NanoLab DualBeam FIB from Material & Structural Analysis Division, Oregon, USA). The processed sample is

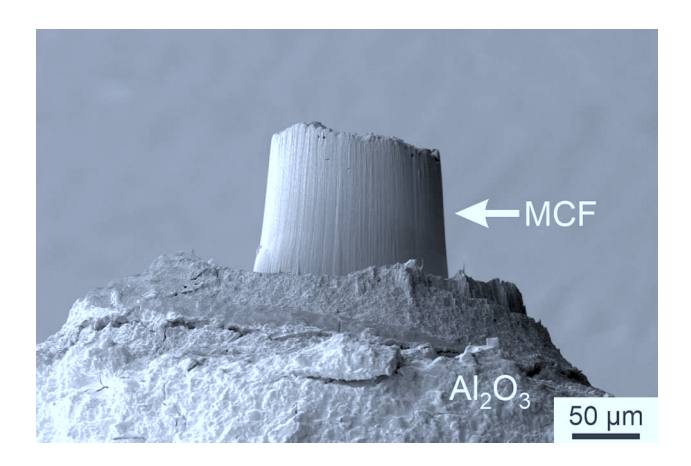


**Figure 1** Scanning electron microscopic image of the APS-MCF sample for the synchrotron measurements after FIB preparation.

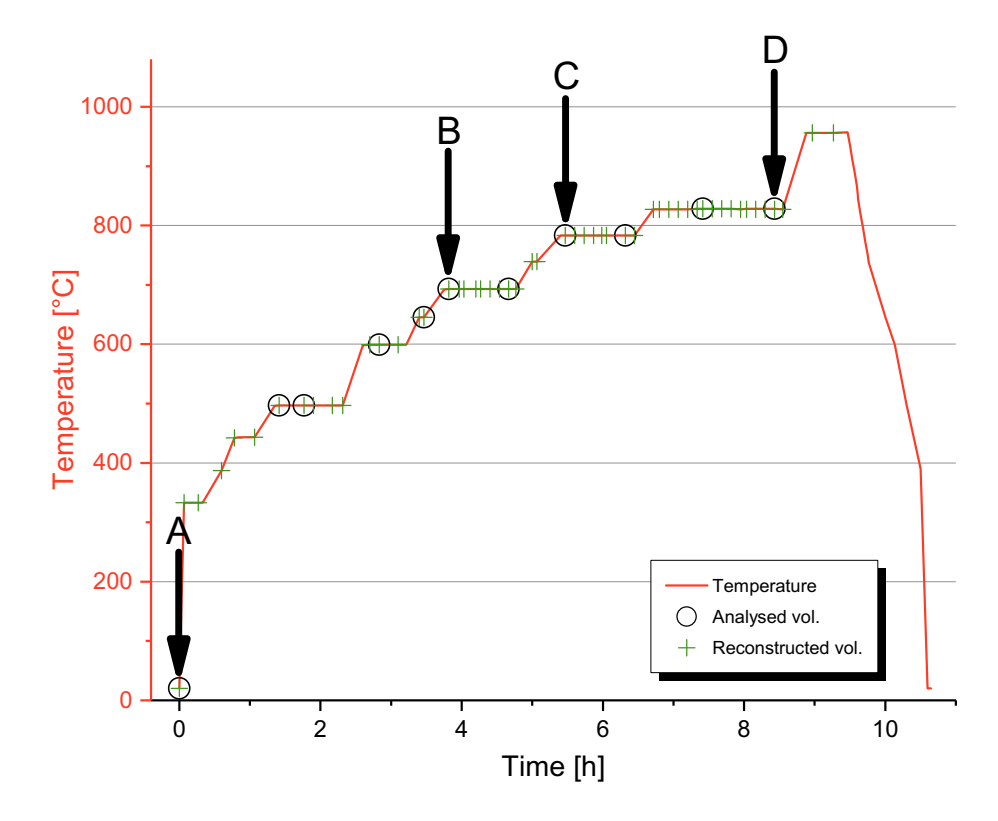
almost cylindrical in shape and has a diameter of 123  $\mu$ m as shown in Fig. 1. The surface of the top of the cylinder is the surface of the free-standing APS-MCF coating the sample was extracted from.

The SXNT in situ measurements were performed at the nano-probe beamline ID16B at the ESRF in Grenoble (France). Acquisition with a pixel size of 75 nm was recorded at the nano-analysis end station ID16B [37] during high-temperature annealing using the furnace available at the beamline [38]. The temperature was controlled via the power of the furnace. To minimize the temperature error, a calibration was performed directly before each measurement using a thermocouple and eutectic samples. The temperature program for the subsequent measurement was used for this purpose (Fig. 2).

It was possible to perform 3D magnified phase contrast imaging during sample annealing within the furnace thanks to carbon glass apertures. A conic pink beam ( $\Delta E/E = 10^{-2}$ ) with an energy of 29.7 keV and a high flux of  $8 \times 10^{10}$  ph s<sup>-1</sup> was used. For each tomographic scan, 1998 projections were acquired on a PCO edge 5.5 camera (2560 × 2160 pixels) along a 360° rotation with an exposure time of 200 ms per step. The total acquisition time per scan was around 7 min. The annealing program is depicted in Fig. 2 and was chosen according to microstructural changes that were observed in ex situ experiments published earlier [23, 31]. 3D reconstructions were achieved in two steps: (1) recursive phase retrieval calculation [39, 40] using an in-house developed octave script based on a Paganin [41] -like approach with a delta/beta of 112 and (2) filtered back projection reconstruction using ESRF software PyHST2 [42].



Figure 2 Temperature profile of the SXNT measurement in red (solid line). Green crosses mark 3D volumes which were reconstructed. Numerically analyzed 3D volumes for porosity calculations are indicated by black circles. The black arrows with the indication A, B, C and D point on different conditions of the sample, where 2D slices of each volume were extracted to visualize changes of the microstructure. They are shown in Fig. 3.



ImageJ [43, 44] and Geodict [45] were applied to analyze qualitatively the 3D volumes reconstructed in the very same sample at different annealing times and temperatures and perform quantitative porosity measurements.

#### **Results**

All reconstructed 3D volumes (indicated with green crosses in Fig. 2) were investigated to select four of them as representatives to summarize all observable microstructural changes during the annealing test. The annealing time at which these four representatives were acquired are indicated with black arrows in Fig. 2. From each of these volumes, a section of the very same cross section, taken at approx. 50 μm from the top of the sample, is given in Fig. 3 to visualize the changes. To choose the very same cross sections of the volumes, pores were used as landmarks. As the surface on top of the cylinder is the same as the surface of the APS-MCF coating, where the sample was extracted from, the images in Fig. 3 are oriented in plane with the coating. The images in Fig. 3 a, b, c and d were taken in the initial state, at a temperature of 693 °C after a total annealing time of 229 min, at a

temperature of 783 °C after a total annealing time of 328 min and at a temperature of 828 °C after a total annealing time of 506 min, respectively. The microcrack indicated by a white arrow in Fig. 3a has a width of 300 to 500 nm in the initial state of the sample. This is a crack opening typically found in plasma-sprayed ceramic coatings [46]. At a temperature of 693 °C after a total annealing time of 328 min, the width of this crack is reduced to 200-300 nm (Fig. 3b). By increasing the temperature and extending the annealing time, this crack is healing completely and cannot be observed in Fig. 3c, d anymore. The black arrow in Fig. 3a draws attention to a pore which is located at the edge of the sample in the initial state. With ongoing annealing, the distance between this pore and the sample edge is increasing (Fig. 3b-d). The images suggest that a layer of material is forming at the surface of the sample, which is in contact with the air atmosphere. Observing the changes of the position of pores to each other during annealing reveals that they do not move significantly. Measurements of the circumference of the sample after different annealing times are given in Table 1. After subtracting the thermally induced expansion, a relative growth of 5.18% is calculated by comparing the initial state and the



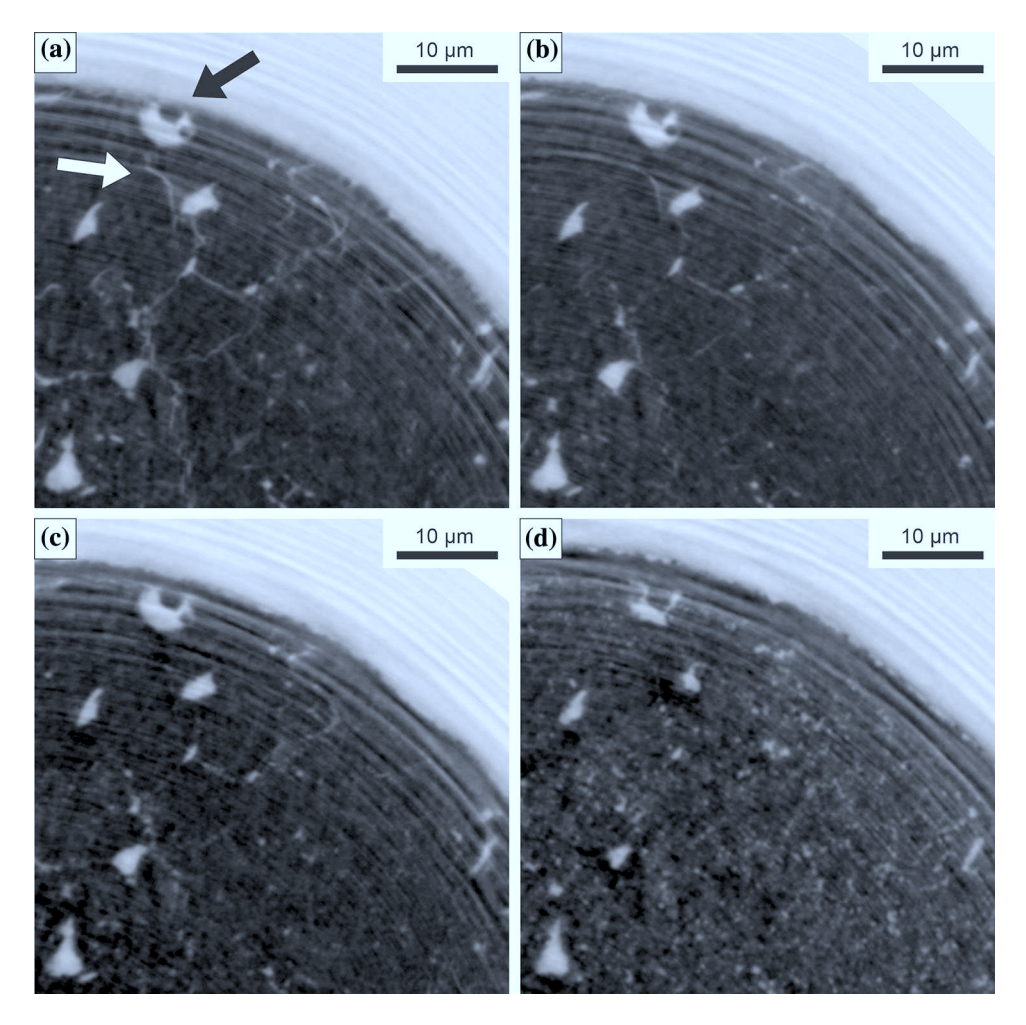


**Figure 3** Selection of the very same cross section within the 3D volumes reconstructed at approx. 50 μm from the top of the very same sample in the initial state (**a**), at a temperature of 693 °C after a total annealing time of 229 min (**b**), at a temperature of 783 °C after a total annealing time of 328 min (**c**) and at a temperature of 828 °C after a total annealing time of 506 min (**d**).

These slices were chosen by using pores as landmarks to find the same sample position. The ring-shaped brightness differences are artifacts coming from the strong phase shift between the material and the air. The black and white arrows mark a pore close to the sample edge and a crack, respectively.

sample at a temperature of 828 °C after a total annealing time of 506 min. The thermal expansion coefficient of MCF between 30 °C and 800 °C, given with  $13.4 \times 10^{-6} \ {\rm K}^{-1}$  in [22], was used in this case.

A closer inspection of images a and d in Fig. 3 revealed an increase in porosity. Small pores with diameters of up to 500 nm are formed in the bulk of the sample during annealing. For porosity measurements, sub-volumes of  $76.92 \times 82.99 \times 98.88 \ \mu m^3$  have been cropped into the full 3D reconstructions. An automated shading correction adjusts the brightness within obtained volumes, and a brightness threshold was set to each volume by eye to distinguish between MCF and cavities (cracks and pores).

Converting the greyscale 32-bit image stacks to binary image stacks along the set thresholds enables quantitative porosity measurements. The porosity values of ten analyzed volumes are given in Fig. 4. After exceeding a temperature of 600 °C, a decrease in the porosity from initially 9% down to 3% can be observed. Setting the threshold has a strong impact on the calculated porosity value and despite the use of a shading correction tool, the images still exhibit a slight shading so that errors occur. By performing each measurement three times with different threshold settings, a porosity error of less than 1.5% is determined and added to the measurement in Fig. 4.



At several parts of the sample, a detachment of an outer layer of material close to the surface can be observed. Figure 5 visualizes this phenomenon with four cross-sectioned slices taken from the 3D volumes at the initial state (a), at a temperature of 783 °C after a total annealing time of 328 min (b), at a temperature of 783 °C after a total annealing time of 379 min (c) and at a temperature of 828 °C after a total annealing time of 506 min (d). The phase transition from material to air at the edge of the sample leads to irregularities in the reconstruction process of the volumes. This is why the material in the center of the images appears darker. Thus, the contrast of the images in Fig. 5 should be evaluated locally. Especially at the edge of the sample, the reconstruction

leads to artifacts in the images. One of these artifacts can be observed as bright, ring-shaped stripes having the samples cylinder axis as center. The cross section of the initial state in Fig. 5a shows cracks (marked with black arrows) at the edge of the sample in the lower part of the image. The annealing leads to a healing of these initial cracks. In accordance with the developments shown in Fig. 3, the formation of a dense layer of material can be observed at the surface of the sample during the annealing. On the right side of images b, c and d in Fig. 5, this layer is detaching from the bulk and has small pores at the inside which are facing the sample. A closer inspection of the tomograms reveals that none of these pores are penetrating the outer part of the shell. It has to be

**Table 1** Measured circumference of the sample at the same position. The last column indicates the relative growth of the circumference with already subtracted thermal expansion (CTE =  $13.4 \times 10^{-6} \text{ K}^{-1}$ ) [22]

Time (min)	Temperature (°C)	Measured circumference (μm)	Relative growth without thermal expansion (%)
0	20	403.5	0
106	497	405.3	0.05
229	693	408.3	0.30
280	693	411.5	1.08
328	783	414.0	2.41
379	783	414.1	3.05
445	828	415.1	4.49
506	828	421.7	5.18

**Figure 4** Porosity measurements performed on the analyzed tomograms are indicated by blue triangles.

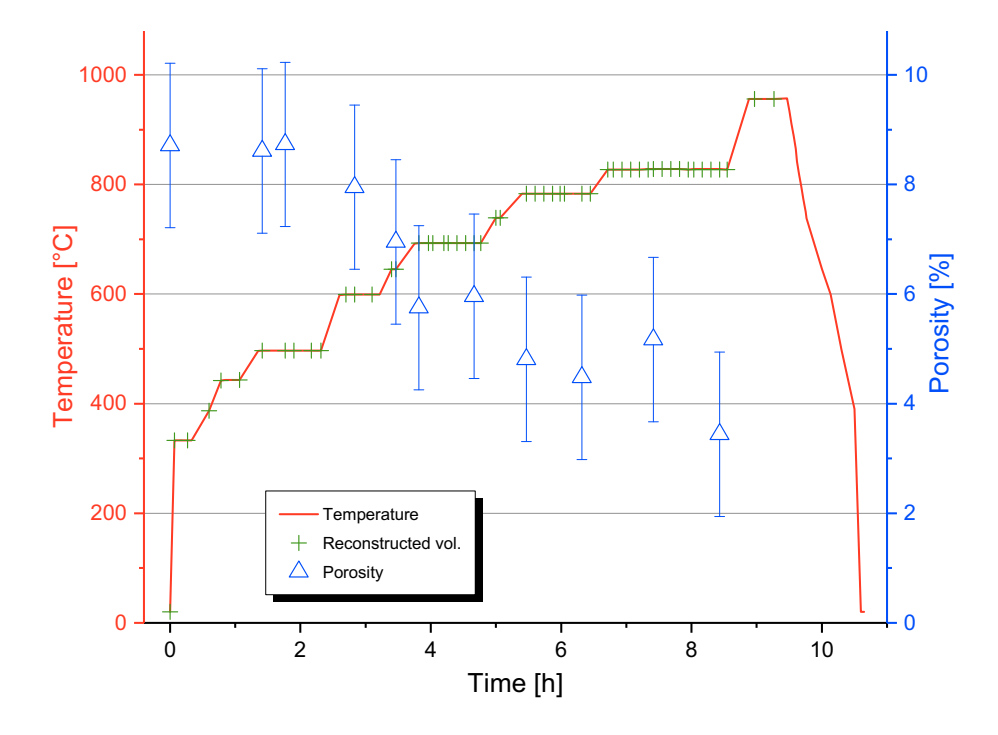
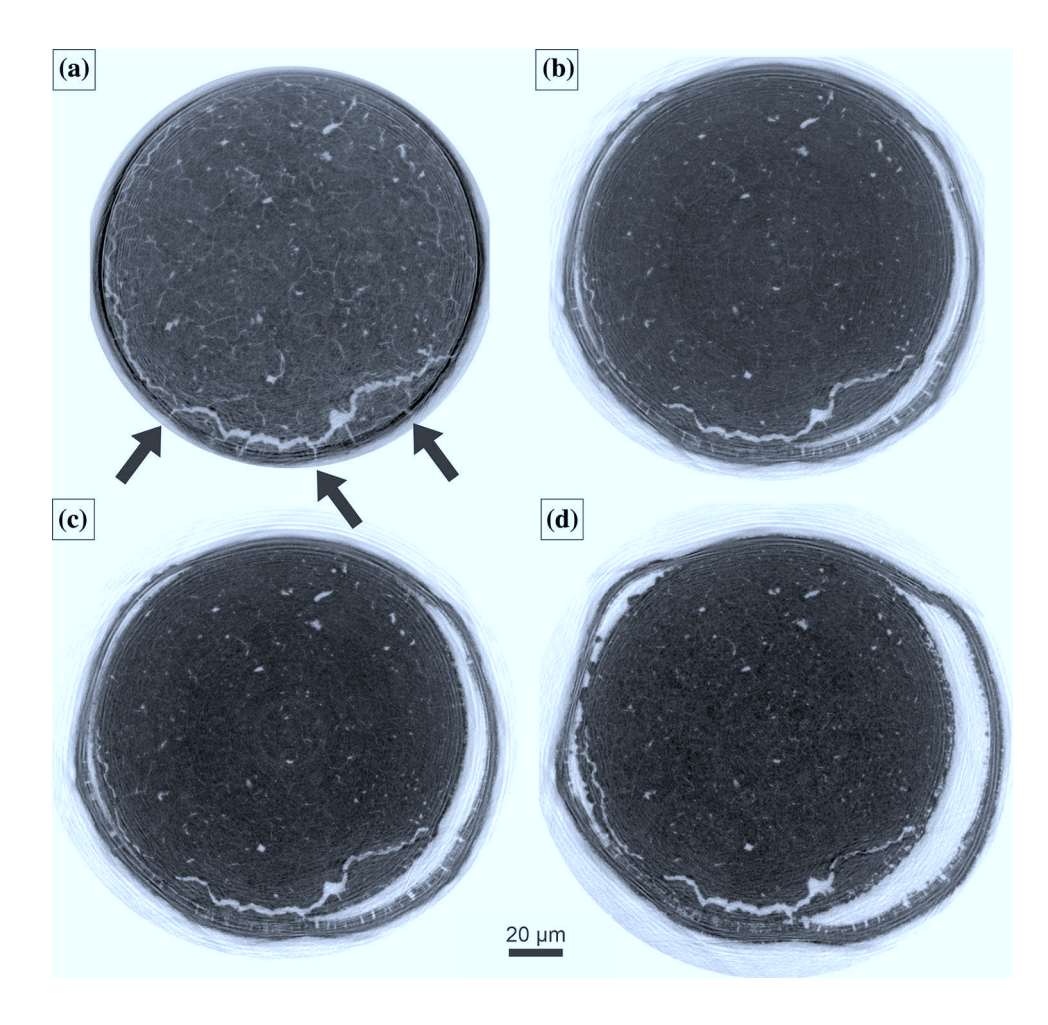




Figure 5 Cross-sectioned slices of the same sample at the same position of the 3D volumes in the initial state (a), at a temperature of 783 °C after a total annealing time of 328 min (b), at a temperature of 783 °C after a total annealing time of 379 min (c) and at a temperature of 828 °C after a total annealing time of 506 min (d). The black arrows mark cracks which are penetrating the surface of the sample in the initial state.



considered that also no cracks can be observed penetrating the detached layer (video in supplementary 2). The layer is a kind of shell which protects the surface of the bulk (underneath the shell) from oxygen. It should be mentioned here that the circumference measurements in Table 1 were performed at a sample position, where the layer detachment did not occur. Comparing the images in Fig. 5 reveals an increase in the length and thickness of this shell during annealing: The circumference increases by 10% comparing the initial state and the image at 828 °C after 506 min. The thickness of the detached layer increases by 23% comparing the sample at 783 °C after 328 min of annealing and at 828 °C after 506 min. A Video showing the microstructural changes during the annealing within transverse cross-section slices is given in Supplementary 3.

#### Discussion

Each sample produced by APS has a unique microstructure, even though the spray process is reproducible. Due to this uniqueness, ex situ observations of microstructural changes by comparing different samples can lead to considerable scatter in the results. The SXNT allows the observation of the microstructural evolution of the same sample. Thus, it can track the changes in situ and is not based on the assumption of similarity. Hypotheses based on ex situ experiments can be proven by this measuring technique.

The crack-healing phenomenon observed in Fig. 3 is consistent with the literature [22, 23, 31]. Due to the limited measuring time at the synchrotron, the annealing time at lower temperatures is shorter compared to the ex situ annealing tests in [23, 31]. A beginning of crack-healing was observed in [23] after an ex situ 180 min annealing at 500 °C. Within the SXNT measurements, a crack-healing was observed



at 693 °C after a total annealing time of 229 min, compared to Fig. 3a, b. The later occurrence of the crack-healing is most likely due to the shorter annealing time at lower temperatures and the lower spatial resolution of the SXNT (compared to a scanning electron microscope). In [23], the mechanism of crack-healing is described by a volume expansion which is induced by a phase transformation from a metastable rock salt configuration  $(Mn,Co,Fe)_1O_1$  to low-temperature the stable spinel (Mn,Co,Fe)<sub>3</sub>O<sub>4</sub>. Since oxygen is required for the phase transformation, this is an oxidation process. The emergence of the metastable rock salt phase is based on quenching of the MCF during the spray process [23].

Ex situ annealing tests of APS-MCF coatings presented in [31] revealed an elemental de-mixing and the formation of a Co-rich spinel oxide layer at the sample surface. Due to this cobalt enrichment, it was assumed that the oxidation proceeds by the outward diffusion of cations via vacancies. Within the SXNT measurements, a further proof of this hypothesis is given by the formation of a layer of material above pores that are located at the edge of the sample. One example is given in Fig. 3, where the pore is indicated with a black arrow. The outward diffusion of cations is accompanied by the inward diffusion of vacancies, which agglomerate and build nano-pores within the bulk. Following the Ostwald ripening process, these nano-pores accumulate to bigger pores, which can be resolved within the 3D volumes in Fig. 3d.

The volume expansion that accompanies the phase transformation at the surface of the APS-MCF layer can induce high mechanical compressive stresses. In an earlier publication, these stresses were estimated by performing curvature measurements of APS-MCF-coated Crofer22APU substrates during annealing in air [22]. However, recent experiments indicate that the actual stress state is a complex interplay of high-temperature relaxation and thermal expansion mismatch stresses [2]. In case of the cylindrically shaped free-standing tomography sample, the missing substrate will have an effect on the stress evolution. In this case, the annular geometry of the spineltype oxide layer redirects the in-layer oriented compressive stresses partly to tensile stresses between the layer and the rock salt bulk. Simultaneously, the vacancy-driven oxidation leads to an increase in the porosity at the boundary between the rock salt and the spinel phase. When the tensile stresses are exceeding a critical value, the spinel layer is detaching from the bulk. The images in Fig. 5, the videos of the full tomogram at 783 °C after a total annealing time of 328 min in Supplementary 2 and the video of the full tomogram at 828 °C after a full annealing time of 506 min in Supplementary 4 show that the detaching spinel layer has a high density and mechanical stability, as no cracks occur penetrating the layer.

Measurements of the size evolution of the detaching layer during annealing within the slice depicted in Fig. 5 reveal a length increase by 5% and a thickness increase by 23% comparing the one at 783 °C after 328 min of annealing and the tomogram at 828 °C after 506 min. It has to be pointed out that the length and thickness increase was measured within the part of the spinel layer that was already detached at 783 °C after 328 min. The tomogram slices, given in supplementary 5, support this observation. Thus, the volume increase cannot be explained by the phase transformation, as the detaching layer is already oxidized. An approach to understand the expansion of the shell is based on the elemental de-mixing during the oxidation. A cobalt enrichment within the emerging spinel layer at the surface of annealed APS-MCF coatings was observed in [31] and could be explained by the differences of the diffusion velocities of Mn, Co and Fe within (Mn,Co,Fe)<sub>3</sub>O<sub>4</sub>. A Corich, cubic spinel layer is formed at the air facing surface of the sample, and a Mn- and Fe-rich tetragonal layer is built up underneath. The crystal structure is dependent on the exact elemental composition and changes over the annealing process. After the full transition to the spinel phase, a re-mixing of elements was observed. Thus, in case of the detached shell within the tomography sample, the re-mixing would start after the detachment inside the shell. Calculating the cell volume based on the measured lattice parameter of the Co-rich spinel at the surface, the Mn-rich tetragonal spinel phase in the bulk and the mixed spinel after long-term annealing presented in [31] lead to no significant change in volume. The exact volumes are 0.594 nm<sup>3</sup> for the tetragonal Mnrich phase, 0.534 nm<sup>3</sup> for the Co-rich spinel and 0.570 nm<sup>3</sup> for the mixed spinel.

Hence, the origin of the length and thickness expansion of the detached layer remains unclear.



#### Conclusion

Coating chromium-containing interconnector steels with APS-MCF protection layers can efficiently reduce Cr-poisoning within SOFCs. During operation, these coatings undergo a phase transformation which lead to strong microstructural changes and elemental de-mixing. In former papers, the basic mechanisms for the observed changes were investigated ex situ after different annealing conditions. Due to the scattering of the microstructure within different samples produced by APS, a certain uncertainty exists with regard to the comparability of these samples. In the present work, the microstructure of one free-standing APS-MCF sample is investigated in situ in three dimensions by applying SXNT at the ID16B beamline at the ESRF. Crack-healing was traced in 3D within the sample after exceeding a temperature of 693 °C. At the surface around the cylindrical sample, the formation of a layer of material was observed growing with increasing annealing time and rising temperature. This underpins the hypothesis that the oxidation of the initial metastable rock salt phase to the stable spinel phase occurs by the outward diffusion of cations, which was set up in [31]. Due to the cationic diffusion by vacancies, these vacancies form small pores and agglomerate to bigger pores. At the sample surface, the emerging spinel shell induces compressive stresses within the shell, which lead to radial tensile stresses between shell and bulk which can lead to the detachment from the bulk. The detached shell seems to be dense and gastight. Further investigations have to be performed to disclose the reason, why the shell is growing in length and thickness within parts that are already detached from the bulk.

## Acknowledgements

Open Access funding provided by Projekt DEAL. The authors gratefully acknowledge the support of Dr. Olaf Medenbach for performing the pre-preparation and Mr. Maximilian Kruth, Forschungszentrum Jülich, Ernst Ruska-Centre for Microscopy and Spectroscopy with Electrons (ER-C) for the fine-tuning of the SXNT sample. The authors would like to thank Dr. Robert Mücke, Forschungszentrum Jülich, Institute of Energy and Climate Research: Materials Synthesis and Processing (IEK-1) for the data

management and assisting with the analyses of the tomograms. We gratefully acknowledge the German Federal Ministry of Education and Research (BMBF) for financing of the project "Verbundvorhaben SOFC Degradation" (Proposal Number 03SF0494A) and the ESRF for its financial support under MA-3254 experiment at the ID16B beamline.

#### **Author contribution**

We confirm that the manuscript has been read and approved by all named authors and that there are no other persons who satisfied the criteria for authorship but are not listed. We further confirm that the order of authors listed in the manuscript has been approved by all of us. We confirm that we have given due consideration to the protection of intellectual property associated with this work and that there are no impediments to publication, including the timing of publication, with respect to intellectual property. In so doing, we confirm that we have followed the regulations of our institutions concerning intellectual property. We understand that the Corresponding Author is the sole contact for the Editorial process (including Editorial Manager and direct communications with the office). He is responsible for communicating with the other authors about progress, submissions of revisions and final approval of proofs. We confirm that we have provided a current, correct email address which is accessible by the Corresponding Author and which has been configured to accept email from nikolas.gruenwald@gmx.net.

### Compliance with ethical standards

**Conflict of interest** We wish to confirm that there are no known conflicts of interest associated with this publication and there has been no significant financial support for this work that could have influenced its outcome.

Electronic supplementary material: The online version of this article (https://doi.org/10.1007/s108 53-020-04916-9) contains supplementary material, which is available to authorized users.

**Open Access** This article is licensed under a Creative Commons Attribution 4.0 International License, which permits use, sharing, adaptation, distribution and reproduction in any medium or format, as long



as you give appropriate credit to the original author(s) and the source, provide a link to the Creative Commons licence, and indicate if changes were made. The images or other third party material in this article are included in the article's Creative Commons licence, unless indicated otherwise in a credit line to the material. If material is not included in the article's Creative Commons licence and your intended use is not permitted by statutory regulation or exceeds the permitted use, you will need to obtain permission directly from the copyright holder. To view a copy of this licence, visit <a href="https://creativecommons.org/licenses/by/4.0/">https://creativecommons.org/licenses/by/4.0/</a>.

#### References

- Boaro M, Arico AS (2017) Advances in medium and high temperature solid oxide fuel cell technology. CISM International Centre for Mechanical Sciences: courses and lectures. Springer, Cham
- [2] Mahato N, Banerjee A, Gupta A, Omar S, Balani K (2015) Review: progress in material selection for solid oxide fuel cell technology. Prog Mater Sci 72:141–337. https://doi.org/ 10.1016/j.pmatsci.2015.01.001
- [3] Quadakkers WJ, Piron-Abellan J, Shemet V, Singheiser L (2003) Review: metallic interconnectors for solid oxide fuel cells. Mat High Temp 20(2):115–127. https://doi.org/10.31 84/096034003782749071
- [4] Molin S, Kusz B, Gazda M, Jasinski P (2008) Evaluation of porous 430L stainless steel for SOFC operation at intermediate temperatures. J Power Sour 181(1):31–37. https://doi. org/10.1016/j.jpowsour.2007.10.009
- [5] Stanislowski M, Wessel E, Hilpert K, Markus T, Singheiser L (2007) Chromium vaporization from high-temperature alloys. J Electrochem Soc 154(4):A295–A306. https://doi. org/10.1149/1.2434690
- [6] Brett DJL, Atkinson A, Brandon NP, Skinner SJ (2008) Intermediate temperature solid oxide fuel cells. Chem Soc Rev 37(8):1568–1578. https://doi.org/10.1039/b612060c
- [7] Beez A, Yin X, Menzler NH, Spatschek R, Bram M (2017) Insight into the reaction mechanism of (La 0.58 Sr 0.40)(Co 0.20 Fe 0.80)O 3-δ cathode with volatile chromium species at high current density in a solid oxide fuel cell stack. J Electrochem Soc 164(10):3028–3034. https://doi.org/10.1 149/2.0051710jes
- [8] Menzler NH, Mai A, Stöver D (2009) Durability of cathodes including Cr poisoning. Handb Fuel Cells. https://doi.org/10. 1002/9780470974001.f500038

- [9] Badwal S, Deller R, Foger K, Ramprakash Y, Zhang J (1997) Interaction between chromia forming alloy interconnects and air electrode of solid oxide fuel cells. Solid State Ionics 99(3–4):297–310. https://doi.org/10.1016/S0167-2738(97)0 0247-6
- [10] Hilpert K (1996) Chromium vapor species over solid oxide fuel cell interconnect materials and their potential for degradation processes. J Electrochem Soc 143(11):3642. h ttps://doi.org/10.1149/1.1837264
- [11] Froitzheim J, Meier GH, Niewolak L, Ennis PJ, Hattendorf H, Singheiser L, Quadakkers WJ (2008) Development of high strength ferritic steel for interconnect application in SOFCs. J Power Sour 178(1):163–173. https://doi.org/10.1016/j.jpowsour.2007.12.028
- [12] Trebbels R, Markus T, Singheiser L (2010) Investigation of chromium vaporization from interconnector steels with spinel coatings. J Electrochem Soc 157(4):B490. https://doi. org/10.1149/1.3298434
- [13] Masi A, Bellusci M, McPhail SJ, Padella F, Reale P, Hong J-E, Steinberger-Wilckens R, Carlini M (2017) Cu–Mn–Co oxides as protective materials in SOFC technology: the effect of chemical composition on mechanochemical synthesis, sintering behaviour, thermal expansion and electrical conductivity. J Eur Ceram Soc 37(2):661–669. https://doi.org/10.1016/j.jeurceramsoc.2016.09.025
- [14] Molin S, Sabato AG, Bindi M, Leone P, Cempura G, Salvo M, Cabanas Polo S, Boccaccini AR, Smeacetto F (2017) Microstructural and electrical characterization of Mn–Co spinel protective coatings for solid oxide cell interconnects. J Eur Ceram Soc 37(15):4781–4791. https://doi.org/10.1016/j.jeurceramsoc.2017.07.011
- [15] da Conceição L, Dessemond L, Djurado E, Souza MMVM (2013) La0.7Sr0.3MnO3-coated SS444 alloy by dip-coating process for metallic interconnect supported solid oxide fuel cells. J Power Sour 241:159–167. https://doi.org/10.1016/j. jpowsour.2013.04.082
- [16] Blum L, de Haart LGJ, Malzbender J, Menzler NH, Remmel J, Steinberger-Wilckens R, de Haart LGJ (2013) Recent results in Jülich solid oxide fuel cell technology development. J Power Sour 241:477–485. https://doi.org/10.1016/j. jpowsour.2013.04.110
- [17] Kiefer T (2007) Entwicklung neuer Schutz- und Kontaktierungsschichten für Hochtemperatur-Brennstoffzellen. Ph.D. Dissertation, University of Bochum
- [18] Choi J-J, Ryu J, Hahn B-D, Yoon W-H, Lee B-K, Park D-S (2009) Dense spinel MnCo2O4 film coating by aerosol deposition on ferritic steel alloy for protection of chromic evaporation and low-conductivity scale formation. J Mater Sci 44(3):843–848. https://doi.org/10.1007/s10853-008-313 2-x



- [19] Shaigan N, Qu W, Ivey DG, Chen W (2010) A review of recent progress in coatings, surface modifications and alloy developments for solid oxide fuel cell ferritic stainless steel interconnects. J Power Sour 195(6):1529–1542. https://doi. org/10.1016/j.jpowsour.2009.09.069
- [20] Saoutieff E, Bertrand G, Zahid M, Gautier L (2009) APS deposition of MnCo<sub>2</sub>O<sub>4</sub> on commercial alloys K41X used as solid oxide fuel cell interconnect: the importance of post heat-treatment for densification of the protective layer. ECS Trans 25(2):1397–1402
- [21] Han SJ, Pala Z, Sampath S (2016) Plasma sprayed manganese–cobalt spinel coatings: process sensitivity on phase, electrical and protective performance. J Power Sour 304:234–243. https://doi.org/10.1016/j.jpowsour.2015.11. 040
- [22] Vaßen R, Grünwald N, Marcano D, Menzler NH, Mücke R, Sebold D, Sohn YJ, Guillon O (2016) Aging of atmospherically plasma sprayed chromium evaporation barriers. Surf Coat Technol 291:115–122. https://doi.org/10.1016/j.s urfcoat.2016.02.005
- [23] Grünwald N, Sebold D, Sohn YJ, Menzler NH, Vaßen R (2017) Self-healing atmospheric plasma sprayed Mn1.0Co1.9Fe0.1O4 protective interconnector coatings for solid oxide fuel cells. J Power Sour 363:185–192. https://doi. org/10.1016/j.jpowsour.2017.07.072
- [24] Kesler O (2007) Plasma spray processing of solid oxide fuel cells. MSF 539–543:1385–1390. https://doi.org/10.4028/w ww.scientific.net/MSF.539-543.1385
- [25] Hui R, Wang Z, Kesler O, Rose L, Jankovic J, Yick S, Maric R, Ghosh D (2007) Thermal plasma spraying for SOFCs: applications, potential advantages, and challenges. J Power Sour 170(2):308–323. https://doi.org/10.1016/j.jpowsour.20 07.03.075
- [26] Franco T, Ruckdäschel R, Lang M, Schiller G, Szabo P (2006) Diffusion and protecting barrier layers in a substrate supported SOFC concept. In: Proceedings 7th international fuel solid oxide cell forum 2006
- [27] Hong J-E, Bianco M, van Herle J, Steinberger-Wilckens R (2015) Properties of spinel protective coatings prepared using wet powder spraying for SOFC interconnects. ECS Trans 68(1):1581–1587. https://doi.org/10.1149/06801.1581 ecst
- [28] Magdefrau NJ, Chen L, Sun EY, Yamanis J, Aindow M (2013) Formation of spinel reaction layers in manganese cobaltite – coated Crofer22 APU for solid oxide fuel cell interconnects. J Power Sour 227:318–326. https://doi.org/10. 1016/j.jpowsour.2012.07.091
- [29] Gannon P, Deibert M, White P, Smith R, Chen H, Priyantha W, Lucas J, Gorokhovsky V (2008) Advanced PVD protective coatings for SOFC interconnects. Int J Hydrogen

- Energy 33(14):3991–4000. https://doi.org/10.1016/j.ijhydene.2007.12.009
- [30] Menzler NH, Sebold D, Guillon O (2018) Post-test characterization of a solid oxide fuel cell stack operated for more than 30,000 hours: the cell. J Power Sour 374:69–76. https://doi.org/10.1016/j.jpowsour.2017.11.025
- [31] Grünwald N, Sohn YJ, Yin X, Menzler NH, Guillon O, Vaßen R (2019) Microstructure and phase evolution of atmospheric plasma sprayed Mn–Co–Fe oxide protection layers for solid oxide fuel cells. J Eur Ceram Soc 39(2–3):449–460. https://doi.org/10.1016/j.jeurceramsoc.20 18.08.027
- [32] Puranen J, Pihlatie M, Lagerbom J, Bolelli G, Laakso J, Hyvärinen L, Kylmälahti M, Himanen O, Kiviaho J, Lusvarghi L, Vuoristo P (2014) Post-mortem evaluation of oxidized atmospheric plasma sprayed Mn–Co–Fe oxide spinel coatings on SOFC interconnectors. Int J Hydrogen Energy 39(30):17284–17294. https://doi.org/10.1016/j.ijhyd ene.2014.08.105
- [33] Aukrust E, Muan A (1963) Phase relations in the system cobalt oxide-manganese oxide in air. J Am Ceram Soc 46(10):511. https://doi.org/10.1111/j.1151-2916.1963.tb137 90.x
- [34] Villanova J, Cloetens P, Suhonen H, Laurencin J, Usseglio-Viretta F, Lay E, Delette G, Bleuet P, Jauffrès D, Roussel D, Lichtner AZ, Martin CL (2014) Multi-scale 3D imaging of absorbing porous materials for solid oxide fuel cells. J Mater Sci 49(16):5626–5634. https://doi.org/10.1007/s10853-014-8275-3
- [35] Olmos L, Bouvard D, Salvo L, Bellet D, Di Michiel M (2014) Characterization of the swelling during sintering of uniaxially pressed copper powders by in situ X-ray microtomography. J Mater Sci 49(12):4225–4235. https://doi.org/ 10.1007/s10853-014-8117-3
- [36] Terzi S, Salvo L, Suéry M, Dahle AK, Boller E (2013) Internal melting and coarsening of liquid droplets in an Al– Cu alloy: a 4-D experimental study. J Mater Sci 48(21):7422–7434. https://doi.org/10.1007/s10853-013-755 7-5
- [37] Martinez-Criado G, Villanova J, Tucoulou R, Salomon D, Suuronen J-P, Labouré S, Guilloud C, Valls V, Barrett R, Gagliardini E, Martínez-Criado G, Suuronen J-P, Dabin Y, Baker R, Bohic S, Cohen C, Morse J (2016) ID16B: a hard X-ray nanoprobe beamline at the ESRF for nano-analysis. J Sync Radiat 23(1):344–352. https://doi.org/10.1107/S1600577515019839
- [38] Villanova J, Daudin R, Lhuissier P, Jauffres D, Lou S, Martin CL, Labouré S, Tucoulou R, Martinez-Criado G, Salvo L, Jauffrès D, Martínez-Criado G (2017) Fast in situ 3D nanoimaging: a new tool for dynamic characterization in



- materials science. Mater Today 20(7):354–359. https://doi.org/10.1016/j.mattod.2017.06.001
- [39] Langer M, Pacureanu A, Suhonen H, Grimal Q, Cloetens P, Peyrin F (2012) X-ray phase nanotomography resolves the 3D human bone ultrastructure. PloS One. https://doi.org/10. 1371/journal.pone.0035691
- [40] Weber L (2016) Iterative tomographic X-Ray phase reconstruction. Ph.D. Dissertation, University of Lyon
- [41] Paganin D (2006) Coherent X-ray optics 6. Oxford University Press on Demand, Oxford
- [42] Mirone A, Brun E, Gouillart E, Tafforeau P, Kieffer J (2014) The PyHST2 hybrid distributed code for high speed tomographic reconstruction with iterative reconstruction and a priori knowledge capabilities. Nucl Instrum Methods Phys Res, Sect B 324:41–48. https://doi.org/10.1016/j.nimb.2013.09.030

- [43] Abràmoff MD, Magalhães PJ, Ram SJ (2004) Image processing with ImageJ. Biophoton Int 11(7):36–42
- [44] Vincent B, Vincent F, Dominique H, Luc S, Pierre L (eds) (2012) Investigating performance variations of an optimized GPU-ported granulometry algorithm. IEEE
- [45] GeoDict. https://www.geodict.de/index.php
- [46] Vaßen R, Traeger F, Stöver D (2004) Correlation between spraying conditions and microcrack density and their influence on thermal cycling life of thermal barrier coatings. J Therm Spray Technol 13(3):396–404

**Publisher's Note** Springer Nature remains neutral with regard to jurisdictional claims in published maps and institutional affiliations.

